ISET Journal of Earthquake Technology, Paper No. 590, Vol. 62, No. 1, March 2025, pp. 1-17

COMPARISON OF IN-SITU AND LABORATORY TEST-BASED SOIL LIQUEFACTION AND CYCLIC SOFTENING RESPONSES

Armin W. Stuedlein (Corresponding Author)
Professor, Oregon State University
Corvallis, OR 97331, USA, E mail id: Armin.Stuedlein@oregonstate.edu

Amalesh Jana
Assistant Professor, Montana State University, Bozeman
MT 59717, USA, E mail id: Amalesh.Jana@montana.edu

ABSTRACT

This paper describes a series of dynamic, *in-situ* tests conducted within natural soil deposits to deduce their seismic and post-seismic responses and presents side-by-side comparison to the results of cyclic and post-cyclic laboratory test programs and/or laboratory test-based models to establish the similarities and differences between the two techniques. The deposits investigated included a low plasticity silt deposit at mean depth of 2.5 m, a moderate plasticity silt deposit at a depth of approximately 10 m, and a medium dense sand deposit at a depth of about 25 m. Two methods for applying seismic loading *in-situ* were deployed: vibroseis shaking and controlled blasting. The *in-situ* seismic responses considered include the variation of maximum and residual excess pore pressure with shear strain and cyclic resistance. Post shaking volumetric strain responses are compared to general and site-specific post-cyclic volumetric strain models for the medium dense sand and medium to high plasticity silt deposits, respectively. The post-shaking monotonic undrained shear strength of the medium to high plasticity silt deposit is compared to a site-specific post-cyclic strength model. Key issues surrounding the differences between laboratory and *in-situ* testing are identified and highlight relevant factors contributing to observed similarities and differences in the observations; these issues include the use of reconstituted specimens and the effects of multidirectional shaking, partial drainage, and excess pore pressure redistribution, all of which are difficult to simulate in the laboratory.

KEYWORDS: Soil Dynamics, Liquefaction, Cyclic Softening, In-Situ Testing

INTRODUCTION

It is exceedingly rare to observe actual earthquake loading in the form of cyclic shear strains or stresses along with the corresponding excess pore pressures. Relating such measurements to the post-seismic performance of soil deposits *in-situ* is likewise infrequent. Laboratory-based evaluation of cyclic and post-cyclic behaviors are readily possible in most fine-grained soils, which can be reliably sampled with reduced disturbance when using best practices (e.g., mud-rotary drilling; piston sampling). However, relatively intact sampling of granular soils with fines contents less than approximately 30 to 50% is significantly challenging. The cost and complexity of retrieving intact samples in these soils often prevents site-specific cyclic and post-cyclic laboratory investigations (e.g., Esposito et al. 2014). Ultimately, laboratory test evaluation of the liquefaction resistance of sandy soils was abandoned in favor of correlations to *in-situ* test data through penetration testing (Seed et al. 1983) and shear wave velocity (e.g., Andrus & Stokoe 2000).

Dynamic *in-situ* testing, pioneered through the use of specially designed instrument arrays and vibroseis mobile shakers at the University of Texas, Austin (Rathje et al. 2001), offers a critical pathway to fill the knowledge gaps separating cause and effect in geotechnical earthquake engineering and to directly evaluate empirical models developed using field and laboratory studies. *In-situ* testing allows large volumes of largely undisturbed soil to be dynamically excited without the impacts of drainage boundary conditions that are necessarily imposed in the laboratory. Some dynamic *in-situ* test techniques can deploy significant magnitudes of seismic energy and are limited to the depths that can be tested solely by the cost of drilling. It has been estimated that tens of millions of dollars (US) have been saved on liquefaction mitigation at one site due to the insights gained through dynamic *in-situ* testing (KGW 2021), yielding an approximate 100:1 return on investment. Dynamic *in-situ* testing has the potential to answer difficult questions, reduce uncertainty, and manage risk in geotechnical practice.

The deposits forming the focus of this study include a low plasticity silt deposit with instruments placed at an average depth of 2.5 m, a moderate to high plasticity silt deposit investigated at a depth of approximately 10 m, and a medium dense sand deposit within an instrument array located at a depth of about 25 m. Two methods for applying seismic loading to *in-situ* instrument arrays were deployed: vibroseis shaking in the low plasticity silt deposit, and controlled blasting in all three deposits. The in-shaking responses considered include relationships between shear strain and maximum and residual excess pore pressure and cyclic resistance with the number of equivalent loading cycles. Post-shaking responses in terms of *in-situ* settlements and volumetric strains are compared to general and site-specific post-cyclic volumetric strain models for the medium dense sand and medium to high plasticity silt deposits, respectively. The *in-situ* post-shaking monotonic undrained shear strength of the medium to high plasticity silt deposit is compared to a site-specific post-cyclic strength model. Key issues surrounding the differences between laboratory and *in-situ* tests are identified and highlight relevant factors contributing to observed similarities and differences in the observations, including the use of reconstituted and intact specimens, and the effects of multidirectional shaking, partial drainage, and excess pore pressure redistribution – effects which are difficult to simulate in the laboratory.

TEST SITES AND SUBSURFACE CHARACTERIZATION

Two test sites form the focus of this study: one at the Port of Portland (PoP), Portland, Oregon and one at the Port of Longview (PoL), Longview, Washington. The subsurface characteristics of both test sites were assessed using downhole and crosshole geophysical tests, mud-rotary boreholes with split-spoon (in sand) and thin-walled tube (in silt) sampling and standard penetration tests (SPTs), cone penetration tests (CPTs), and an array of laboratory tests ranging from basic characterization tests to constant rate of strain consolidation, monotonic and cyclic direct simple shear testing, and post-cycling testing. The subsurface characteristics of the PoP site include 5 to 6 m of dredged sand and silty sand fill overlying an approximately 2 m thick alluvial loose sand layer, which is underlain by a 5 to 6 m thick medium stiff plastic silt (ML and MH) deposit. Below the silt deposit and extending to depths greater than 30 m is deposit of alluvial, medium dense, clean sand and sand with silt (SP and SM). The groundwater table varied from approximately 3 to 7 m over the course of the project due to changes in the adjacent Columbia River stage and dewatering associated with construction at the port. The reader is referred to Jana & Stuedlein (2021a, 2022) for specific details regarding explorations and subsurface conditions at the PoP.

The subsurface characteristics of the PoL site includes a thin (0.4 m) layer of fill (dense silty sand with gravel), underlain by approximately 1 m of medium stiff sandy silt (ML) transitioning to soft clayey silt and silty clay (ML and CL), in turn underlain by a 1.2 m thick layer of very soft to soft clayey silt to silty clay (MH and CH) and a deep deposit of very soft to medium stiff clayey silt (ML) with thin lenses of sandy silt extending to the base of the explorations. CPTs and pore pressure transducers placed within the depths ranging from approximately 2 to 3 m indicated a groundwater table of approximately 1.45 m in the period spanning the explorations and *in-situ* dynamic testing. The reader is referred to Jana et al. (2023) and Dadashiserej et al. (2024a) for a detailed description of the subsurface conditions at the PoL. Together, the instruments placed at these test sites offer insights into the *in-situ* responses of a shallow low plasticity silt (PoL), a deeper medium plasticity silt (PoP), and a deep deposit of medium dense sand (PoP), as described herein.

DESIGN AND EXECUTION OF DYNAMIC *IN-SITU* TEST PROGRAMS

1. Port of Portland (PoP) Test Site

The overall design of the *in-situ* dynamic experiments included several key components: (1) instruments placed in mud-rotary boreholes including triaxial geophone packages (TGPs), pore pressure transducers (PPTs), and inclinometer casing fitted with sondex settlement rings; and (2) boreholes fitted with PVC casings to place explosives at pre-determined depths which, upon detonation, generated body waves to excite the soils within the instrument arrays. Figure 1 presents key aspects of the experimental design and programs conducted at the PoP site. The Silt Array (Figure 1b) included two strings of three TGPs to measure particle velocity at depths ranging from 9 m to 11.45 m set on a vertical spacing of 1.22 m, three PPTs to measure hydrostatic and excess pore pressures at depths ranging from 9.5 to 10.67 m set on a spacing of 0.5 and 0.67 m, and sondex settlement rings. The TGPs in the Silt Array were used to form two main 2D "finite" elements, including Element 1 (TGPs S3, S4, S6, and S7) and Element 2 (TGPs S4, S5, S7, and S8; Figure 1b). Two additional elements were formed to assess the effect of element shape and make use of PPT 5 (Figure 1b): Elements 3 and 4 were formulated as rhombus-shaped elements comprising TGPs S8, S4, S3, and S7, and TGPs S7, S5, S4, and S6, respectively. The Sand Array included two strings of three TGPs at depths ranging from 23.8 m to 26.2 m set on a vertical spacing of 1.22 m, three PPTs at depths ranging from 24.4 to 25.6 m set on a spacing of 0.61 m, and sondex settlement rings, with a geometry (not shown) similar to that deployed in the Silt Array. The TGPs in the Sand Array were used to form 2D Element 1 (TGPs S10, S11, S13, and S14) and Element 2 (TGPs S9, S10, S12, and S13).

Three distinct blasting events were carried out at the PoP site: the Test Blast Program (TBP), the Deep Blast Program (DBP), and the Shallow Blast Program (SBP). The TBP was carried out using 8 charges varying in weight (kg, TNT-equivalent) from 0.23 to 3.63 kg (Figure 1a) and was intended to check the settings of the data acquisition system, evaluate attenuation of surface wave amplitudes, and provide the baseline crosshole shear wave velocity, Vs. The DBP was carried out on the day following the TBP and included 30 charges placed as shown in Figure 1a with charge weights ranging from 0.09 to 3.65 kg and detonation delays as shown in Figure 1c. The main goal of the DBP was to excite the deep medium dense sand deposit and Sand Array. The SBP was carried out on the third day and likewise included 30 charges (Figure 1a) with charge weights ranging from 0.09 to 1.83 kg and 1 second delays between successive detonations (Figure 1d), with the main goal of exciting the medium stiff plastic silt deposit and Silt Array. The Sand and Silt Arrays recorded particle velocities and pore pressures during each of the three blast programs. Refer to Jana et al. (2021) for details regarding the fabrication and installation of the instruments, and Jana & Stuedlein (2021a, 2022) for details regarding the dynamic responses of the Sand and Silt Arrays, respectively.

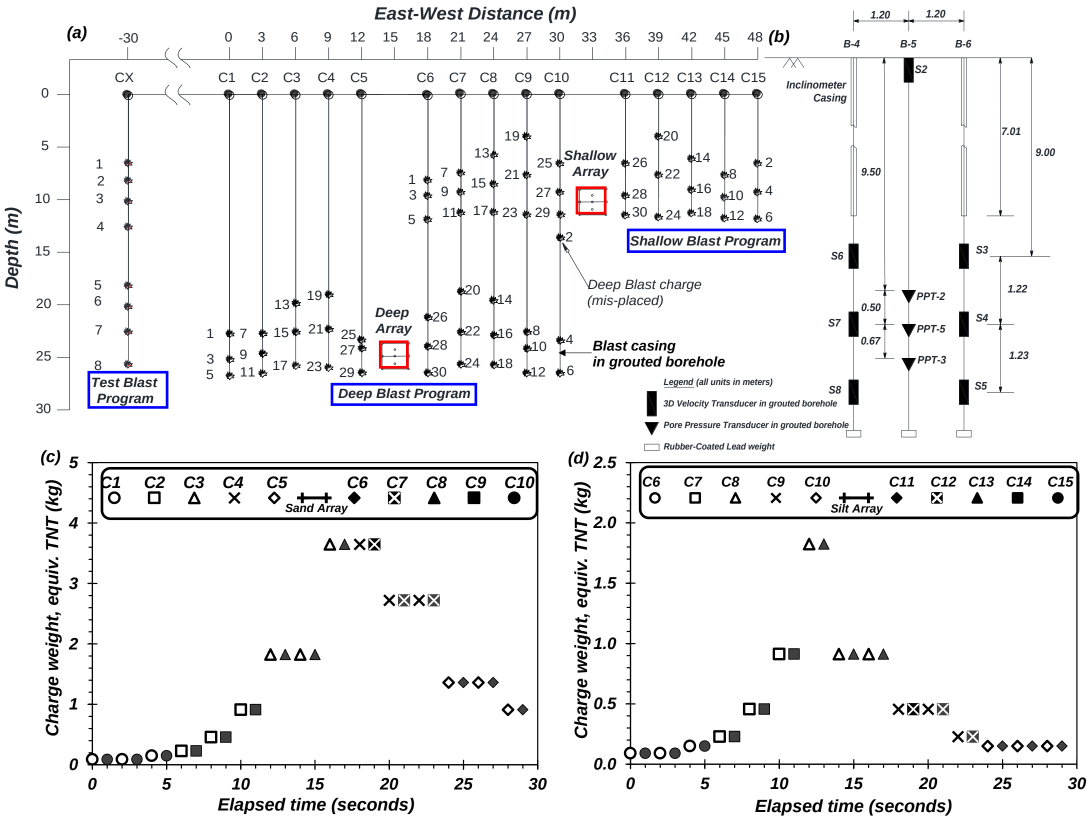

Fig. 1 Details of the experimental controlled blasting programs at the PoP site: (a) elevation view of the blast and instrumentation arrays showing the as-built locations of each charge used in each of the three blast events; (b) elevation view of the as built Silt Array; (c) schematic of the Deep Blast Program (DBP) indicating charge detonation time history for explosives distributed within blast casings C1 through C10 (d) detonation time history conducted during the Shallow Blast program (SBP) within blast casings C6 through C10 and C11 through C15 (modified after Jana 2021)

2. Port of Longview (PoL) Test Site

The experimental *in-situ* test program at the PoL site (Figure 2) consisted of two modes of dynamic shaking of an instrument array, termed the OSU Silt Array, using: (1) the NHERI@UTEXAS vibroseis shaker truck T-Rex (Stokoe et al. 2017), and (2) the controlled blasting technique. Vibroseis shaking was conducted first owing to the anticipated small to moderate levels of shear strain imposed and consisted of five shaking events (Stages 1 through 5), each of which consisted of the application of uniaxial sinusoidal

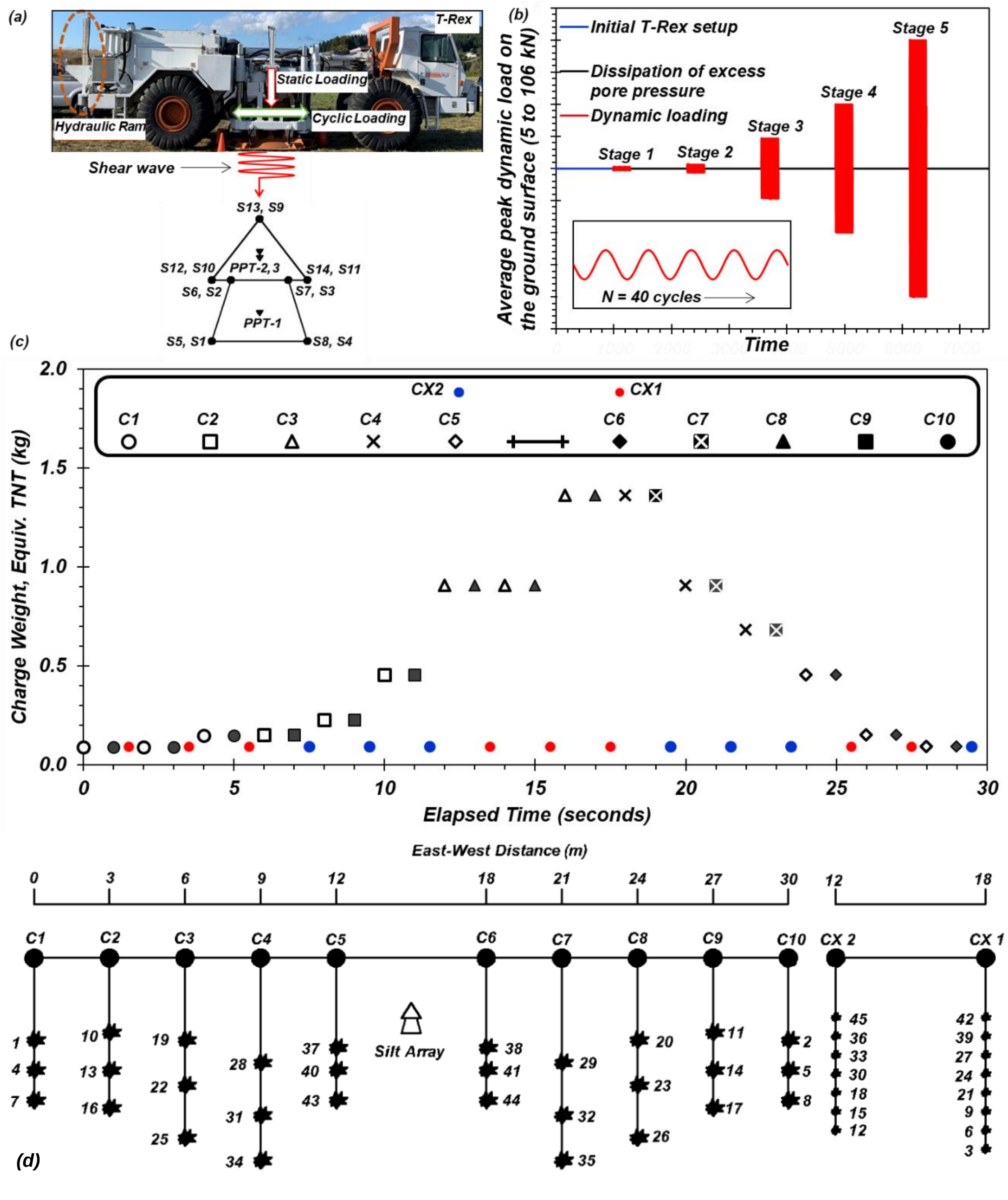

Fig. 2 Details of the experimental controlled blasting programs at the PoL site: (a) schematic of T-Rex and loading of the Silt Array, (b) shaking stages with increasing amplitudes of loading, (c) detonation sequence and charge weights, and (d) elevation view of the blast array, aligned East-West displaying the as-built location of each charge within blast casings (modified after Jana 2021)

motion for 4 seconds with a loading frequency of 10 Hz (Figure 2b). The base plate of T-Rex, through which the shaking motion is transferred to the subsurface, was placed over and aligned with the truncated, pyramid-shaped solid three-dimensional (3D) Element 2, which consisted of TGPs S1, S2, S3, S4, S5, and S6. The base plate partially overlaid the triangular prism-shaped 3D Element 1 which was constructed using

TGPs S9, S10, S11, S12, S13, and S14. Uniaxial shaking was conducted in the east-west direction, aligned with blast casings C1 through C10 as detailed below, to force maximum velocity amplitudes along the east-west (or "x") component of each TGP. The controlled blasting experiment proceeded the following day after all excess pore pressures had dissipated, using a novel detonation sequence (Figure 2c) and charge distribution (Figure 2d). Casings CX1 and CX2 were positioned north of the instrument array and equipped with small, 0.09 kg charges intended to interrogate the Silt Array and measure the small-strain V_s between the detonation of larger charges. Casings C1 through C10 housed charges ranging from 0.09 to 1.36 kg in order to trigger nonlinear elastic and nonlinear inelastic dynamic responses. Refer to Jana et al. (2023) for additional details regarding the experimental program for the PoL site.

GROUND MOTION CHARACTERISTICS, ANALYSIS, AND COMPARISON TO LABORATORY ELEMENT TESTS

The shaking motion produced by the T-Rex base plate, while predominantly uniaxial and horizontal with constant frequency (i.e., 10 Hz), can produce rocking motions consisting of both horizontally- and vertically-polarized, vertically propagating ground motions (Zhang 2020). Thus, the full six-component, 3D Cauchy strain tensor was computed directly from the TGPs using finite element analysis of particle displacements derived from the velocity measurements. The frequency content of blast-induced P- and S-waves, however, are not constant and vary continuously through the experiment: P-waves are characterized by frequencies in the hundreds to thousands of hertz (Jana et al. 2021b; Jana et al. 2022; Jana et al. 2023) and pass in a largely drained state in accordance with the compression wave theory by Ishihara (1968). The frequency of the P-wave tends to increase as charges are detonated closer to the array due to the reduced material volumes through which the motion can attenuate. On the other hand, two types of S-waves are produced: (1) due to the unloading of the P-wave as the wavefront passes a given sensor (i.e., the near-field S-Wave), and (2) due to the initial disturbance at the location of the charge (i.e., the far-field S-Wave; Sanchez-Salinero et al. 1986). These waves are characterized by much lower initial frequencies which progressively reduce as the soil softens under dynamic shear excitation. The blast-induced S-waves generated in these experimental programs are characterized by frequencies which are shared by earthquake ground motions and typically range from approximately 10 to 50 Hz over the course of an experiment (Jana et al. 2021b; Jana et al. 2022). Although blast-induced ground motions are irrefutably 3*D*, the ground motions can be assumed to be represented by 2D plane waves when blast casings are aligned with the geophones and the source-to-site (or charge-to-instrument) distance is sufficiently large (e.g., at the PoP site; Jana et al. 2021b, Jana et al. 2022, Stuedlein et al. 2023). In the case of the blast experiment at the PoL, all body waves were examined as 3D ground motions and the full 3D Cauchy strain tensor was computed.

In order to compare computed *in-situ* strains and the corresponding excess pore pressures, u_e, to that observed in laboratory element tests, it was necessary to adopt a common measure of strain. In the case of the medium dense sand deposit at the PoP site, split-spoon samples of material were reconstituted to the same relative density, D_r (approximately 50%) and V_S (218 m/s) at the *in-situ* vertical effective stress, σ'_{v0}= 240 kPa and subject to strain-controlled, constant volume cyclic direct simple shear (CDSS) tests. Thin-walled tube samples derived from each silt deposit (i.e., at the PoP and PoL sites) were used to prepare intact, constant volume monotonic direct simple shear (DSS) and CDSS test specimens to evaluate key cyclic and post-cyclic responses of the soils from the instrumented deposits. To make comparisons of *in-situ* and laboratory test results on the basis of a common stress path, the *in-situ* Cauchy strains were first converted to the octahedral shear strain (Chang 2011):

$$\gamma_{oct} = \left(\frac{2}{3}\right)\sqrt{\left(\varepsilon_{xx}-\varepsilon_{yy}\right)^2+\left(\varepsilon_{yy}-\varepsilon_{zz}\right)^2+(\varepsilon_{zz}-\varepsilon_{xx})^2+\frac{3}{2}\left(\gamma_{zx}{}^2+\gamma_{xy}{}^2+\gamma_{yz}{}^2\right)} \tag{1}$$

where ε_{xx}, ε_{yy} and ε_{zz} are the normal strains in the *x*, *y* and *z* directions, and γ_{zx} , γ_{xy} and γ_{yz} are the shear strain components of the 3D Cauchy strain tensor. The constant-volume $\gamma_{DSS,eq}$ could then be calculated by setting normal strains equal to zero using (Cappa et al. 2017):

$$\gamma_{DSS,eq} = \sqrt{\frac{3}{2}}\,\gamma_{oct} \tag{2}$$

The use of Eq. (2) allows direct comparison of the *in-situ* shear strains to those developed from laboratory CDSS tests.

COMPARISON OF *IN-SITU* AND LABORATORY-BASED SHEAR STRAIN-EXCESS PORE PRESSURE MEASUREMENTS

1. Dynamic, *In-Situ* Observations

The understanding of the *in-situ* generation of maximum, $u_{e,max}$, and residual excess pore pressure, $u_{e,r}$, with shear strain is critical for improving the fundamental understanding of liquefaction triggering as well as calibration of constitutive models for forward nonlinear dynamic analysis (NDAs). Herein, $u_{e,max}$ is defined as the maximum shear-induced u_e, measured during passage of cyclic S-waves (T-Rex) and near- and far-field transient S-waves (controlled blasting). In contrast, $u_{e,r}$ is defined as the shear-induced u_e at the end of any given loading cycle (T-Rex) and in the quiescent period immediately following passage of the far-field S-wave (controlled blasting). The maximum and residual excess pore pressure ratio, $r_{u,max}$ and $r_{u,r}$ defined as the ratio of $u_{e,max}$ and σ'_{v0}, and $u_{e,r}$ and σ'_{v0}, respectively, can then be paired with the maximum DSS-equivalent shear strain, $\gamma_{DSS,max}$, to develop the *in-situ* shear strain-excess pore pressure relationships for each instrument array.

Figures 3a and 3b present the $\gamma_{DSS,max}$-$r_{u,max}$ and $\gamma_{DSS,max}$-$r_{u,r}$ data derived from the Sand Array (PoP) during the TBP and DBP, respectively. Whereas no residual excess pore pressures were measured in Element 2 of the Sand Array following the TBP, Element 1 experienced $r_{u,r}$ of 0.3% corresponding to the peak $\gamma_{DSS,max}$ of 0.0134% and $r_{u,max}$ = 4.7%. Owing to the exceedance of the threshold shear strain to trigger excess pore pressure, γ_{tp}, corresponding to the initiation of the nonlinear inelastic constitutive regime in Element 1, the post-dissipation V_s in Element 1 decreased from 225 m/s to 192 m/s, indicating some damage to the soil fabric resulting from shear wave passage. Execution of the DBP (Figures 1a and 1c) led to the triggering of significant excess pore pressures with $r_{u,max}$ of 72 and 64% and peak $\gamma_{DSS,max}$ of 1.37% and 1.2% in Elements 1 and 2, respectively (Figures 3a and 3b). Due to drainage under high, local hydraulic gradients following Blast #22 (Element 1) and Blast #27 (Element 2), development of greater u_e was prevented during the DBP.

Figures 3c and 3d present the $\gamma_{DSS,max}$-$r_{u,max}$ and $\gamma_{DSS,max}$-$r_{u,r}$ data deduced within the Silt Array (PoP) during the TBP, DBP, and SBP, respectively. The maximum shear strain during the three controlled blasting tests was 0.33% corresponding to $r_{u,max}$ = 24% as observed in Element 1 during the SBP. In contrast, the peak shear-induced $r_{u,max}$ of 31% was observed twice: once in Element 2 corresponding to $\gamma_{DSS,max}$ of 0.2% in the DBP and again corresponding to $\gamma_{DSS,max}$ of 0.11% in the SBP. Comparison of the $\gamma_{DSS,max}$-$r_{u,r}$ relationships shown in Figure 3d shows that the medium plasticity, medium stiff Silt Array exhibited greater sustained $r_{u,r}$ in the SBP, a possible effect of the large inelastic shear strain excursions experienced during the DBP. Dadashiserej et al. (2022) and Jana et al. (2025) describe the effects of small and large pre-straining on the cyclic and dynamic responses of silty soils.

Figures 3e and 3f present the $\gamma_{DSS,max}$-$r_{u,r}$ data deduced within the Silt Array (PoL) during controlled blasting and staged T-Rex loading for N = 10 and 40 cycles, respectively. The inset figure in Figure 3f shows that the 40 cycles of Stage 1 loading did not produce excess pore pressures, $r_{u,r}$ > 0%. However, $\gamma_{DSS,max}$ of 0.0097% and 0.0145% was achieved during Stage 2 loading (N = 40) in Elements 1 and 2, respectively, indicating that γ_{tp} was exceeded during this stage. The maximum $r_{u,r}$ for N = 10 and 40 cycles observed during T-Rex loading with $\gamma_{DSS,max}$ = 0.11% was 10% (Figure 3e), and 16.5% (Figure 3f), respectively, in Element 1 following Stage 5 loading. In contrast, the peak $\gamma_{DSS,max}$ = 0.15% was observed in Element 2, located directly below the T-Rex base plate. The excess pore pressures generated in Element 1 were greater than Element 2 in part due to the greater multidirectional loading experienced as a result of the position of the T-Rex base plate. That $r_{u,r}$ was greater in Element 1 is attributed to the migration of u_e within the deeper low plasticity silt layer towards the higher plasticity silt layer within which the upper portion of Element 1 was situated. Thus, dynamic *in-situ* testing can capture the effect of both multidirectional ground motions and system responses of soils (e.g., Cubrinovski et al. 2019). Figures 3e and 3f present the strain cycle-independent $\gamma_{DSS,max}$-$r_{u,r}$ relationships developed from the controlled blasting test conducted at the PoL Silt Array; blasting produced significantly larger shear strains and excess pore pressures, with $\gamma_{DSS,max}$ = 1.14% and a corresponding $r_{u,r}$ of 61%. Jana et al. (2023) compare the response of the low plasticity silt deposit to the shear strains and excess pore pressures from the silty sand Wildlife instrument array during the 1987 Superstition Hills earthquake deduced by Zeghal & Elgamal

(1994); the correlation between the two sets of $\gamma_{DSS,max}$-$r_{u,r}$ data, and sand-like behavior observed in CDSS tests on intact specimens from the PoL site, clearly illustrate that the instrumented low plasticity silt deposit is sand-like and susceptible to liquefaction.

2. Comparison of *In-Situ* and Laboratory-Based Observations of γ_{DSS}-r_u

The value of large-strain, dynamic, *in-situ* testing becomes apparent when comparing to laboratory element test data on reconstituted and intact specimens. Figure 3a compares the $\gamma_{DSS,max}$ - $r_{u,max}$ relationships between the PoL Sand Array and the excess pore pressure model proposed by Cetin & Bilge (2012), which was developed using 185 stress-controlled cyclic triaxial and CDSS tests, for the D_r of the medium dense sand deposit. The excess pore pressure model underpredicts $r_{u,max}$ over nearly the entire

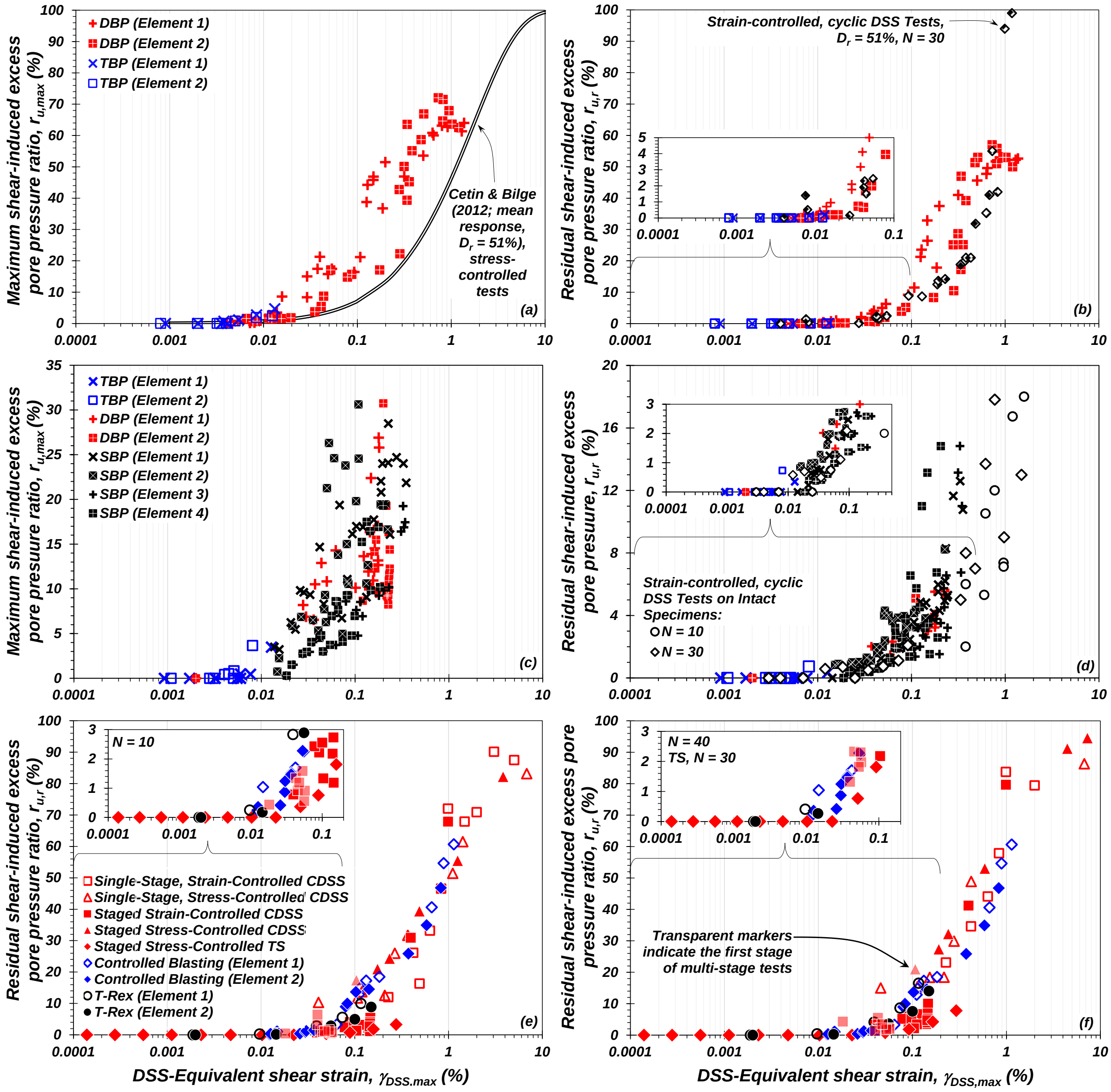

Fig. 3 *In-situ* and laboratory-based maximum DSS-Equivalent shear strain and excess pore pressure relationships: (a) $r_{u,max}$ for the Sand Array (PoP), (b) $r_{u,r}$ for the Sand Array (PoP) with $N = 30$ (lab), (c) $r_{u,max}$ for the Silt Array (PoP), (d) $r_{u,r}$ for the Silt Array (PoP) with $N = 10$ and 30 (lab), (e) $r_{u,r}$ for the Silt Array (PoL) with $N = 10$ (lab, T-Rex), and (f) $r_{u,r}$ for the Silt Array (PoL) with $N = 30$ (TS) and $N = 40$ (CDSS, T-Rex). Note: there is no N corresponding to blast data. Data from Jana & Stuedlein (2021a, 2022) and Dadashiserej et al. (2024a)

range in shear strain imposed during the DBP for blasts where drainage had not yet initiated. The under-prediction in $r_{u,max}$ stems from two critical differences between the *in-situ* and laboratory test data: (1) the database used to calibrate the Cetin & Bilge (2012) model included reconstituted specimens subject to stress-controlled cyclic testing, only, and (2) the soil response to shear waves is more fundamentally linked to induced shear strains, rather than shear stresses (Dobry et al. 1982; Seed et al. 1983; Dobry & Abdoun 2015). Figure 3b shows that CDSS specimens of sand retrieved from the Sand Array and consolidated to the same D_r, V_s, and σ'_{v0} as the conditions in the Sand Array and subjected to strain-controlled, constant volume shearing with f = 0.1 Hz produce better agreement in terms of $\gamma_{DSS,max}$-$r_{u,r}$, for moderate strains ranging from approximately 0.1 to 0.8%. However, the deviations observed in Figure 3b are expected owing to the use of reconstituted soils which cannot capture the *in-situ* soil fabric, multidirectional loading, and redistribution and migration of excess pore pressures during shaking (Jana & Stuedlein 2021a).

Figure 3d compares the $\gamma_{DSS,max}$-$r_{u,r}$ relationships observed *in-situ* at the PoP Silt Array to the results of strain-controlled, constant-volume CDSS tests conducted on intact specimens retrieved from the Silt Array and consolidated to their *in-situ* σ'_{v0} = 106 kPa. For nearly all shear strains, the *in-situ* $r_{u,r}$ is larger than that of the intact specimens for both N = 10 and 30, despite being sheared under constant-volume (i.e., comparable to undrained) loading. This may confirm that the mud-rotary drilling, piston sampling, careful handling and specimen preparation techniques implemented for this study may induce sufficient sample disturbance to reduce the brittleness of intact soils, as noted by many others. However, the role of variability in plasticity and fines content from specimen to specimen, each of just ~20 mm height and 70 mm diameter, may also contribute to the differences observed to the large-scale Silt Array. It is concluded that, compared to the cyclic laboratory test results, the *in-situ* observations are of greater reliability and representativeness of the deposit as a whole and naturally reflect the response of a significantly larger volume of soil.

Considering the comparative response of the low plasticity silt deposit at the Port of Longview, Figures 3e and 3f presents the results of single- and multi-stage, stress- and strain-controlled, cyclic DSS and multi-stage, undrained, stress-controlled torsional shear (TS) test (conducted in collaboration with Professors Kenneth H. Stokoe II and Brady Cox, and Dr. Zhongze Xu) against the staged T-Rex and controlled blasting *in-situ* test data. In contrast to the observations of the medium stiff, medium plasticity Silt Array at the Port of Portland, the comparison between *in-situ* and cyclic laboratory test data for the Silt Array at the Port of Longview is remarkably good, especially for $\gamma_{DSS,max}$ > 0.15% and N = 10. However, for smaller shear strains, the response of the Silt Array is generally more brittle with greater excess pore pressure sensitivity to straining than the laboratory element test specimens at N = 10 as shown in the inset figures. Considering the *in-situ* response to controlled blasting, as the duration of loading and strains increase, the $\gamma_{DSS,max}$-$r_{u,r}$ relationships derived from the constant-volume and undrained, uniaxial cyclic element tests and N = 40 produce greater sensitivity to shear strain amplitude. This may suggest that the role of partial drainage and thus increased cyclic resistance during *in-situ* testing could outweigh the effect of multidirectional shaking for these low plasticity silt soils.

COMPARISON OF *IN-SITU* AND LABORATORY-BASED CYCLIC RESISTANCE

1. Calculation of *In-Situ* Cyclic Shear Stresses

It is rather uncommon to observe actual earthquake loading, excess pore pressure, and cyclic resistance of soil deposits *in-situ*. Indeed, most liquefaction case histories which are used to develop liquefaction triggering relationships (e.g., Cetin et al. 2018, Kayen et al. 2013, Boulanger & Idriss 2016) have been developed using estimates of peak ground acceleration. Deployment of the vibroseis shaking and controlled blasting techniques offer approaches to specify directly or indirectly, respectively, and measure the magnitude of cyclic loading of instrumented soil deposits. In the case of T-Rex loading, the ability to calculate the cyclic shear stresses, τ_{cyc}, depends on the predominant dimensionality of ground motions. At the PoL site, it was determined that Element 2, situated directly under the T-Rex base plate, was subjected to predominantly longitudinal (i.e., x) motion which facilitated the reasonable assumption that the element was subjected to plane wave loading (Dadashiserej et al. 2024a). This assumption allowed the implementation of the Joyner & Chen (1975) formulation for dynamic shear stress for any particular component of motion, i, $\tau_{cyc,i}$, given by:

$$\tau_{cyc,i} = \rho \cdot v_i \cdot V_s(\gamma) \quad (3)$$

where ρ = soil density, v_i = the particle velocity of a given component, and the governing shear wave velocity which varies with the amplitude of shear strain within any given dynamic excursion and is computed using the average downhole V_s during cyclic loading. The shear stress was computed for each orthogonal component (i.e., *x*, *y*, *z*) of sinusoidal motion and at each node (i.e., TGP) in Element 2 of the PoL Silt Array and averaged over 40 loading cycles, which was then used to calculate the vector resultant τ_{cyc} at each node. The global average shear stress over all nodes was then selected as the representative τ_{cyc} over N = 40 and the observed level of cyclic resistance in terms of $r_{u,max}$ (Dadashiserej et al. 2024a). The cyclic stress and resistance ratios, *CSR* and *CRR*, respectively, could then be computed through normalization of τ_{cyc} by σ'_{v0}. Note that for any given cyclic failure criterion, *CSR* = *CRR* at "failure," specified herein in terms of $r_{u,max}$.

Blast-induced ground motions contain a wider range in body wave types and frequencies than vibroseis motions. An analysis of the motions recorded in the DBP and SBP at the Port of Portland by Stuedlein et al. (2023) demonstrated that the predominant frequency of blast motions was dominated strongly by S-waves. Further, the frequency of the P-waves were so large that the shockwave moves essentially through the porewater alone (Ishihara 1968) and do not result in relative slip of soil particles, a necessary requirement for the generation of residual excess pore pressure (Martin et al. 1975; Dobry et al. 1982). Therefore, the particle velocities measured at each node could be justifiably filtered using a low-pass 70 Hz filter. Stuedlein et al. (2023) also demonstrated that the majority of the blast-induced ground motions at the PoP site could be treated as 2D motions owing to the linear arrangement of blast casings (Figure 1a), installation of 2D instrument arrays, and the relatively large source-to-site distances. These three conditions served to produce shared velocity amplitudes and phases for any pair of vertically adjacent TGPs. Thus, once conditioned to remove P-waves, individual particle velocities and large-strain V_s was used in the Joyner & Chen (1975) formulation (i.e., Eq. 3) to compute τ_{cyc} and *CSR*. The *CSR* time history was paired with typical cycle counting procedures developed for earthquake ground motions (e.g., Idriss & Boulanger 2006; Verma et al. 2019) to link *CSR* to the equivalent number of loading cycles, N_{eq}, for each charge detonated. Refer to Stuedlein et al. (2023) for further details on ground motion processing and interpretation.

Figure 4 presents several examples of the longitudinal (*x*) and transverse (i.e., vertical, *z*) *CSR* time histories and selected *CSR* waveforms for individual blasts at the Sand and Silt Arrays at the PoP site. The ranges in maximum *CSR* are large, spanning 0.01 to 0.36 and 0.02 to 0.46, in the Sand and Silt Arrays, with average *CSR*s of 0.15 and 0.19, respectively. Their amplitudes vary as a function of charge weight and distance and are transient, not unlike earthquake ground motions, despite the 1 second delays between charges and differences in frequency content. The individual waveforms shown in the inset figures demonstrate varying degrees of multidirectional shaking produced through controlled blasting. The total number of cycles with varying amplitude and *CSR* > 0.01 was 49 and 86 for the Sand and Silt Arrays, respectively; the corresponding equivalent number of cycles was computed through assessment of reference *CSR*s as described by Idriss & Boulanger (2006).

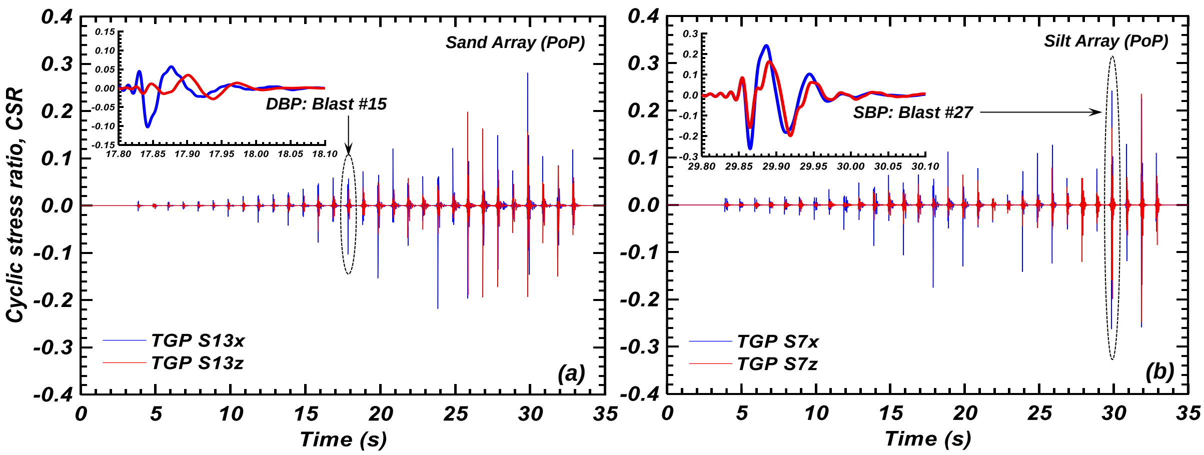

Fig. 4 Example *CSR* time histories derived from longitudinal (x) and transverse (x) particle velocities: (a) *CSR* corresponding to TGP S13 in the Sand Array (PoP) during the DBP, and (b) *CSR* corresponding to TGP S7 in the Silt Array (PoP) during the DBP. Note the frequency content of the *S*-waves for selected charges (i.e., about 15 to 20 Hz). Data reported by Stuedlein et al. (2023)

2. Comparison of *In-situ* and Laboratory-based Observations of *CRR-N*

Comparison of the *in-situ* and laboratory-based cyclic resistances must be made on a common basis, i.e., a common cyclic failure criterion. For any cyclic failure criterion, the *CRR* may be expressed as (Boulanger & Idriss 2015):

$$CRR = a \cdot N^{-b} \tag{4}$$

where a is a fitted constant and corresponds to the *CRR* for N = 1 and b is the empirical semi-logarithmic slope of the curve. The maximum excess pore pressure ratio observed in the Sand Array during the DBP was 72%; thus, the available stress-controlled, constant-volume CDSS test data described above was reinterpreted to produce the relationship between *CRR* and the number of loading cycles corresponding to $r_{u,max}$ = 72%. Figure 5a shows that the *CRR-N* curves for the cyclic failure criteria of $r_{u,max}$ = 72% and the more common γ_{DSS} = 3% are nearly identical for the reconstituted medium dense sand specimens, with a and b equal to 0.20 and 0.125, respectively, for the latter criterion. Comparison of the *in-situ* and laboratory-based cyclic resistances is therefore reasonable. Figure 5a demonstrates that: (1) the *in-situ* $CRR\text{-}N_{eq}$ curve for Element 1 is larger than that of Element 2, due to the lower $r_{u,max}$ generated, and (2) the *in-situ* sand is characterized by notably greater cyclic resistance than that of the laboratory specimens for a given N. For example, for N = 15 and associated with a moment magnitude, M_w = 7.5, the *in-situ* *CRR* = 0.22 and is approximately 50% greater than that of the reconstituted sand specimens (*CRR* = 0.14). It should be noted that the laboratory-based *CRR* has not been reduced by 10% to account for multi-directional shaking effects (Idriss & Boulanger 2008). These observations agree well with the *CRRs* of frozen and cored, and unfrozen sampled sands with $D_r \approx 50\%$ reported by Yoshimi et al. (1984). However, partial drainage affected the *in-situ CRR* as documented by Stuedlein et al. (2023).

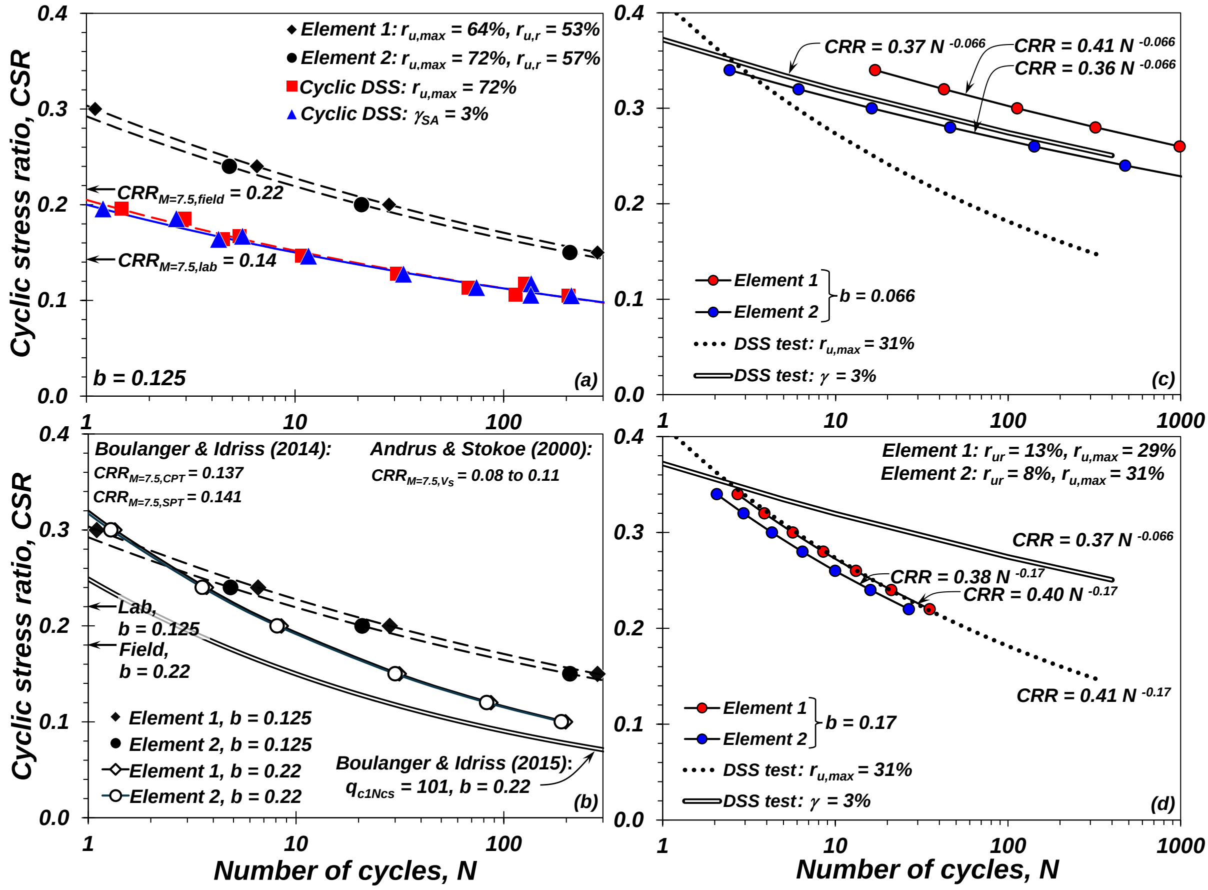

Fig. 5 *In-situ* cyclic resistance derived from controlled blasting experiments: (a) variation of *CRR-N* in Sand Array (PoP) Elements 1 and 2 with laboratory-derived b = 0.125 with comparison to CDSS test specimens, and (b) comparison of *CRR-N* in Sand Array assuming b = 0.125 and 0.22 to various *in-situ* test-based liquefaction triggering relationships; (c) variation of *CRR-N* in Silt Array (PoP) Elements 1 and 2 with laboratory-derived b = 0.066 with comparison to CDSS test specimens, and (d) assuming $r_{u,max}$- and $r_{u,r}$-compatible exponent b = 0.17. Data from Stuedlein et al. (2023)

An alternate approach to determine N_{eq} for the DBP and Sand Array was evaluated to overcome potential limitations of the use of reconstituted sand specimens to develop exponent b, since b can vary significantly for sands depending on the relative density, soil fabric, cementation, and other factors (Boulanger & Idriss 2015; Verma et al. 2019). The mean overburden stress- and fines-content corrected cone tip resistance, q_{c1Ncs}, in the Sand Array was 98, which corresponds to an exponent b of approximately 0.22 in the relative density- and CPT-based estimates of cyclic resistance by Boulanger & Idriss (2015). Figure 5b presents a comparison of case history- and *in-situ* test-based *CRRs* for N = 15 and M_w = 7.5 (Boulanger & Idriss 2014, 2016; Andrus & Stokoe 2000), and the *CRR-N* curve for the CPT-based liquefaction triggering model by Boulanger & Idriss (2016). The V_S-based *CRRs* range from 0.08 to 0.11 and are well below that deduced from the *in-situ* dynamic test when considering either estimate of b. In contrast, the CPT- and SPT-based triggering procedures yielded $CRR_{M=7.5}$ that are approximately 21 to 35% smaller than *in-situ* cyclic resistance for b = 0.22 and 0.125, respectively. A comparison of probabilistic model estimates and *in-situ CRRs* is described by Stuedlein et al. (2023).

In contrast to the sands within the Sand Array, the soils within the PoP Silt Array could be sampled in an intact state and tested directly to establish their cyclic resistance. The results of a detailed cyclic testing program on these soils are reported by Jana & Stuedlein (2021b), and the representative *CRR-N* curve for γ_{DSS} = 3% is shown in Figure 5c, with a low exponent b = 0.066 due its moderately high *PI* (Dadashiserej et al. 2024b). However, because the maximum shear strain in the Silt Array was 0.35%, the cyclic test data was reinterpreted to produce a *CRR-N* curve corresponding to $r_{u,max}$ = 31%, characterized with b = 0.17 (Figures 5c and 5d), which clearly results in lower cyclic resistance for the majority of loading cycles, as expected. The exponents b for γ_{DSS} = 3% and $r_{u,max}$ = 31% were used to calculate the *in-situ* CRR-N_{eq} curves for the blast-induced ground motions, and are compared in Figures 5c and 5d, respectively. Clearly, the *in-situ CRR* depends strongly on the curvature of the selected laboratory *CRR-N* curve and the selection must be justified on the basis of shear strain amplitude or excess pore pressure. In the case of the Silt Array, use of the r_u-consistent laboratory curve in Figure 5d is the most appropriate. For this case, the *CRR* for N = 30 and corresponding to M_w = 7.5 ranges narrowly between 0.215 and 0.225 for Elements 1 and 2, or about 75% of that of the *CRR* developed using intact samples and the γ_{DSS} = 3% cyclic failure criterion. Note that the effects of multidirectional shaking to reduce cyclic resistance is intrinsically included in the *in-situ* CRR-N_{eq} curves for the two elements, which produce *CRR* which are smaller by 0 to 7% than the uniaxial cyclic test results interpreted using $r_{u,max}$-consistent N. This finding is consistent with prior recommendations for reducing the *CRR* by 4% for plastic soils to account for multidirectional shaking (e.g., Idriss and Boulanger 2008).

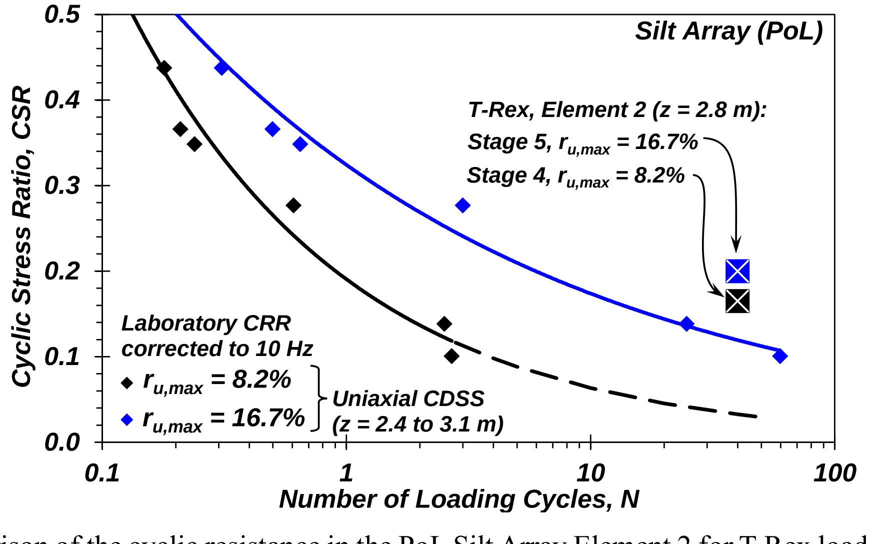

Fig. 6 Comparison of the cyclic resistance in the PoL Silt Array Element 2 for T-Rex loading Stages 4 and 5 with CDSS test results on intact specimens at the same maximum excess pore pressure ratio, $r_{u,max}$

Figure 6 presents the comparison of the *in-situ* cyclic resistance of the low-plasticity PoL Silt Array derived for near-planar T-Rex loading of Element 2 to the results of stress-controlled, constant-volume CDSS tests interpreted for two field-consistent, $r_{u,max}$-based quasi-cyclic failure criteria (i.e., $r_{u,max}$ = 8.2 and 16.7%). The laboratory-based *CRR* was corrected from a loading frequency of 0.1 Hz to 10 Hz for direct comparison to the *in-situ CRR* by increasing the *CRR* by 18%. For the lowest $r_{u,max}$, the laboratory-based *CRR-N* curve was extrapolated to avoid introducing potential error to the cyclic test results due to the low effective consolidation stress and friction within the CDSS apparatus (Dadashiserej et al. 2024a). In this comparison, no assumption regarding exponent b was necessary due to the direct specification of uniform sinusoidal loading in the field. The *in-situ* cyclic resistance is clearly larger than that of the $r_{u,max}$-consistent *CRR*, by a factor of five and 1.67 for T-Rex loading Stages 4 and 5 and for N = 40 (Figure 6). In contrast to the results of the controlled blasting experiments at the PoP site, partial drainage did not occur during T-Rex loading such that it did not contribute to the observed cyclic resistance.

COMPARISON OF *IN-SITU* AND LABORATORY-BASED POST-CYCLIC VOLUMETRIC STRAIN

In addition to assessing the cyclic resistance of soil deposits *in-situ*, dynamic testing can also be used to assess the accuracy of post-shaking settlement estimates following dissipation of excess pore pressures. The PoP Sand and Silt Arrays included grouted inclinometer casings fitted with a corrugated, flexible sheathing pipe and sondex settlement rings, which were monitored prior to and following controlled blasting. The top of the casing was surveyed using a digital optical level, and the settlement rings were surveyed using an inductance probe, the latter of which has an accuracy of no better than 6 mm. Settlement of approximately 7 mm was measured at the ground surface and the base of the sondex casings following

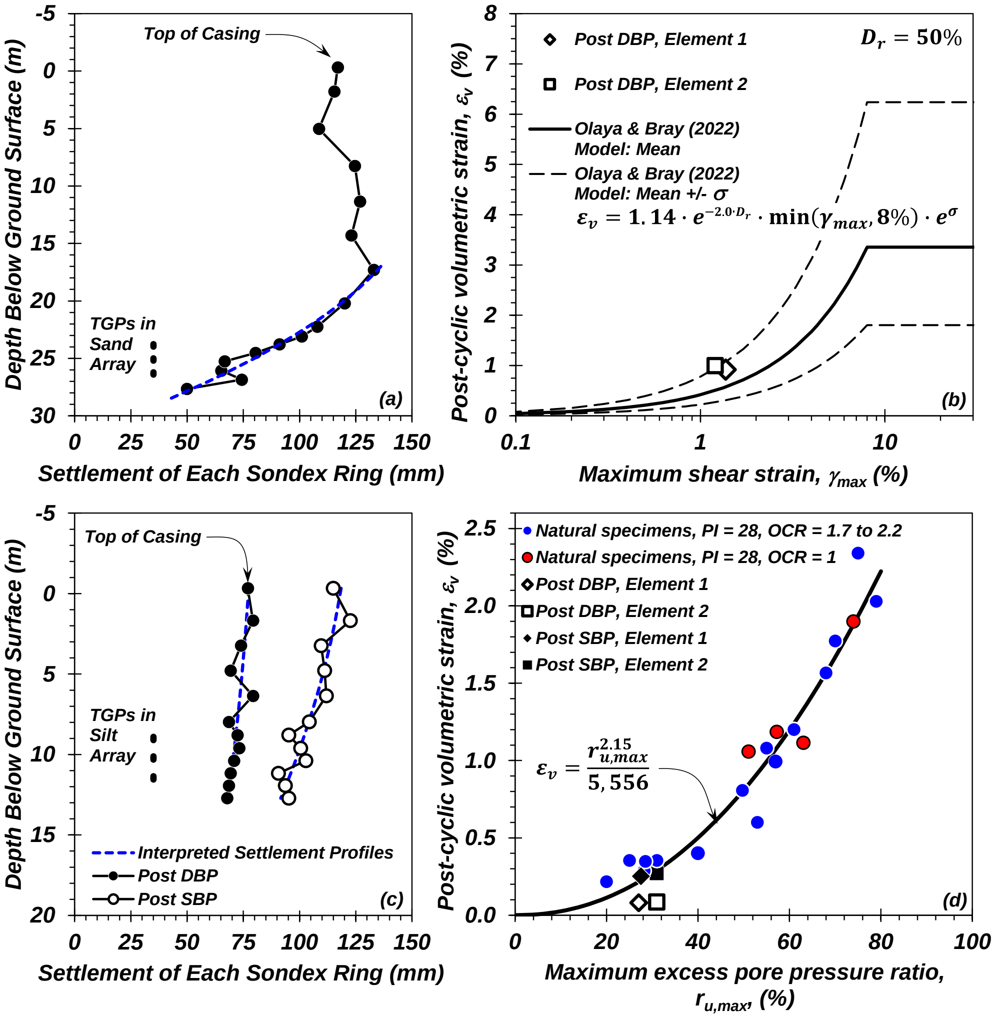

Fig. 7 Comparison of measured *in-situ* post-shaking volumetric strains to that volumetric strain models: (a) settlement profile measured in the Sand Array (PoP) following the DBP, (b) comparison of measured volumetric strains to that of the Olaya & Bray (2022) model, (c) settlement profiles measured in the Silt Array (PoP) following the DBP and SBP, and (d) comparison of measured *in-situ*, post-shaking volumetric strains to the site-specific volumetric strain model based on intact specimens reported by Jana & Stuedlein (2021b)

the TBP (not shown), indicating that all settlement occurred within the deep medium dense sand deposit for the first blast event. Owing to the similarity in instrument accuracy and measured settlement, the settlement profiles at the two instrument arrays are not presented herein for the TBP. The settlement profiles measured following dissipation of excess pore pressures in both the Sand and Silt Arrays following the DBP (Sand Array) and DBP and SBP (Silt Array) are shown in Figures 7a and 7c, respectively, along with settlement profiles interpreted from the relatively noisy sondex data.

The medium dense sand deposit settled about 125 mm following the DBP, with approximately 23 mm of settlement occurring within the Sand Array (i.e., over depths ranging from 23.77 to 26.21 m). This translated to volumetric strains, ϵ_v, of approximately 0.92% and 1.0% in Elements 1 and 2, respectively (Figure 7b). The maximum shear strain-driven post-liquefaction volumetric strain model by Olaya & Bray (2022) is presented in Figure 7b for comparison to the measured volumetric strains, along with the mean estimate +/- the model standard deviation (σ = 0.62). The Olaya & Bray (2022) model was based on the post-cyclic volumetric strains measured following cyclic triaxial and direct simple shear tests on soils reported in 20 research studies, with relative density, coefficients of uniformity, C_u, and fines contents, FC, that span the conditions in the medium dense sand deposit (i.e., D_r = 50%, C_u ranging from 1.8 to 5.1; FC ranging from 3 to 12%). The model produces estimates of ϵ_v equal to 0.57% and 0.50%, for the imposed $\gamma_{DSS,max}$ of 1.37% and 1.2% in Elements 1 and 2, respectively, or approximately half of that observed and falling near the mean + σ estimate. It is worthwhile to point out that $r_{u,max}$ did not exceed 72% and $\gamma_{DSS,max}$ was just greater than one-third of that typically assumed to represent liquefaction in sands. Although model error may contribute to the mean underestimate of the observed ϵ_v, it should be noted that the model was developed considering uniaxial cyclic loading. Pyke et al. (1975) have demonstrated that sands subject to multidirectional shaking, such as described herein, can produce ϵ_v that are up to three times larger than that of uniaxial shaking, depending on the cyclic stress ratio. Seed et al. (1978) adopted a factor of two to account for the effects of multidirectional shaking on volumetric strain.

With regard to the post-shaking deformation response within the Silt Array, the majority of settlement occurred in the medium dense sand deposit below the array during both events, with a total of 2 and 6.5 mm of settlement from the depths of 9 to 11.45 m (Figure 7c). The settlement profiles interpreted from the sondex measurements were used to compute the volumetric strain following the DBP and SBP, as shown in Figure 7d. The volumetric strain in both elements was approximately 0.08% following the DBP, and 0.25 and 0.27% following the SBP. The measured *in-situ* post-cyclic ϵ_v following the SBP are in good agreement with the site-specific volumetric strain model, developed using intact CDSS test specimens derived from samples retrieved from the Silt Array and reported by Jana & Stuedlein (2021b), whereas ϵ_v measured following the DBP was smaller than that of the laboratory specimens by a factor of three.

The differing outcomes observed between the comparison of measured and estimated post-shaking volumetric strains in the Sand and Silt Arrays may stem from differences in the model formulations. Specifically, the Olaya & Bray (2022) model selected uses γ_{max} as the independent variable driving ϵ_v whereas the site-specific model by Jana & Stuedlein (2021b) uses $r_{u,max}$. If $r_{u,max}$ can be estimated in forward analyses that account for multidirectional shaking, it is likely to produce more accurate estimates ϵ_v as the generation of excess pore pressure is a direct indicator of fabric damage, which gives rise to the amount of strain during reconsolidation. Indeed, the scatter in site-specific relationships between γ_{max} and ϵ_v for low (Dadashiserej et al. 2022) and medium to high (Jana & Stuedlein 2021b) plasticity silts has been observed to be greater than that for $r_{u,max}$. For plastic fine-grained soils, it can be concluded that post-cyclic volumetric strain models using maximum excess pore pressure and developed from intact specimens can provide accurate to potentially conservative (in the case of the DBP), estimates of post-shaking settlements.

COMPARISON OF *IN-SITU* AND LABORATORY-BASED POST-CYCLIC MONOTONIC UNDRAINED STRENGTH

Another potential benefit of dynamic *in-situ* testing is the evaluation of post-shaking strength loss, critical for normally- and lightly-overconsolidated, plastic, fine-grained soils, such as those within sloping ground or below shallow foundations. Figure 8a presents the results of post-cyclic, constant-volume, monotonic DSS tests conducted on intact specimens retrieved from the PoP Silt Array at a strain rate of 5%/hour. The degradation of post-cyclic undrained shear strength, $s_{u,pcy}$, varies with the magnitude of excess pore pressure generated during the cyclic stage, which serves as a proxy for damage to soil fabric. Within the specimen-to-specimen variability, a clear trend of decreasing mobilized shear stress and $s_{u,pcy}$, defined as the shear stress mobilized at 15% strain, with increasing $r_{u,max}$ may be observed (Figure 8b). Prior to the execution of the blast programs at the Port of Portland, a 9 m deep borehole approximately 1.2 m from the Silt Array was drilled, cased, and filled with drilling mud and water to the ground surface. This borehole served to provide immediate post-SBP access to a skid rig-mounted vane shear test (VST) apparatus to facilitate *in-situ* shear strength testing. Although rod friction below 9 m served to render deep VST results unreliable, the first two tests where the total measured rod friction was the smallest were successful and yielded $s_{u,pcy}$ = 39 and 38 kPa at the depths of 9.64 and 10.14 m, respectively. These post-shaking strengths correspond to $r_{u,max}$ of 31% and $r_{u,r}$ ranging from 12.5 to 17.5% and correlate well with the post-cyclic monotonic DSS test results on the same material. Figure 8b also compares the laboratory and *in-situ* test results to the model of post-cyclic strength presented by Ajmera et al. (2019) for normally-consolidated reconstituted plastic soils; the over-consolidated soils (i.e., $OCR \approx 2$) within the Silt Array exhibit greater post-cyclic strength owing to their more developed natural soil fabric and increased lateral stress, although the rate of decrease in strength is comparable. It is concluded that post-cyclic strength models developed from intact specimens can provide suitable estimates of post-shaking undrained shear strength in plastic, fine-grained soils.

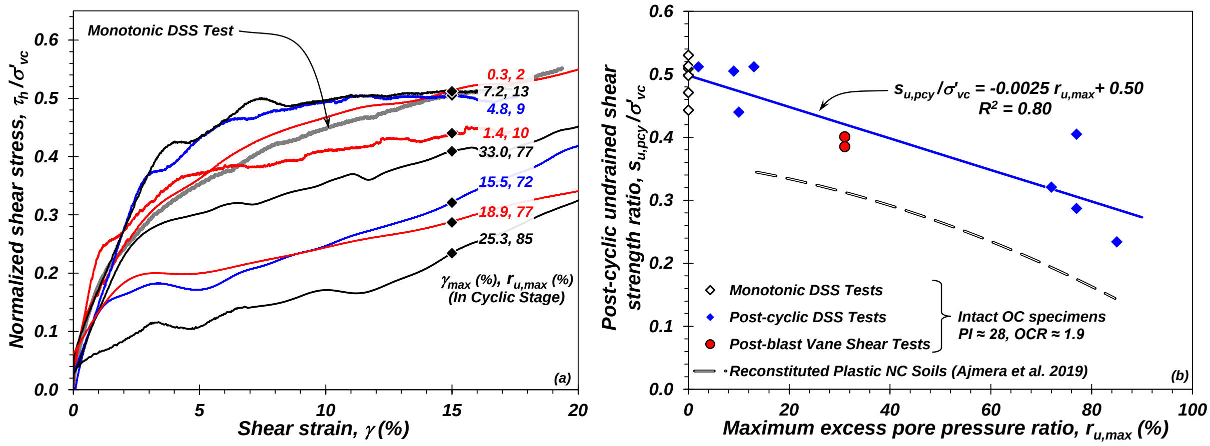

Fig. 8 Role of maximum excess pore pressure in available post-cyclic undrained shear strength: (a) variation of post-cyclic monotonic undrained shear strength as a function of maximum shear strain and $r_{u,max}$ for intact DSS specimens, and (b) comparison of post-blasting *in-situ* vane shear strength to post-cyclic DSS test results (data from Jana & Stuedlein 2022)

CONCLUDING REMARKS

This paper described a series of dynamic, *in-situ* tests conducted within natural soil deposits to deduce their seismic and post-seismic responses and presents side-by-side comparison to the results of cyclic and post-cyclic laboratory test programs to establish the similarities and differences between the two techniques. The deposits investigated included a low plasticity silt deposit at mean depth of 2.5 m, a moderate to high plasticity silt deposit at a depth of approximately 10 m, and a medium dense sand deposit at a depth of about 25 m. Two methods for applying seismic loading *in-situ* were deployed: vibroseis shaking and controlled blasting. The main benefit of vibroseis shaking is the specification of uniform sinusoidal cyclic loading at the ground surface, which allows for direct comparison to cyclic tests after correcting for potential rocking motions as described herein. In contrast, the main benefit of controlled blasting is the ability to dynamically load any type of soil, at any depth, and to shear strains exceeding 1%. A methodology to convert particle velocities to shear strains associated with the direct simple shear stress path and available techniques to convert transient ground motions to the number of equivalent loading cycles allow direct comparison to laboratory test results. Both approaches allow for the direct comparison of the obtained data to models developed for excess pore pressure generation, liquefaction triggering, and cyclic softening in order to assess their accuracy to predict the response of natural soil deposits to earthquake loading. The addition of other testing techniques further allows post-seismic responses to be measured, including volumetric strain and strength, critical for the assessment of the consequences of liquefaction and cyclic softening.

ACKNOWLEDGMENTS

Thanks are due to Professor T. Matthew Evans, Professor Kenneth H. Stokoe, Professor Brady R. Cox, Dr. Ali Dadashiserej, Dr. Benchen Zhang, and Dr. Zhongze (Steve) Xu for their collaboration at the Port of Longview site and fruitful discussions. The authors were supported by the National Science Foundation (Grant CMMI 1663654) during the course of experiments conducted at the Port of Longview. The authors also gratefully acknowledge the sponsorship of this work by Cascadia Lifelines Program (CLiP) and its members, with special thanks to member agency Port of Portland and Port Engineer Tom Wharton, P.E., for the studies conducted at the Port of Portland. Any opinions, findings, and conclusions expressed are those of the authors and do not necessarily reflect the views of the above-mentioned sponsors.

REFERENCES

1. Andrus, R.D. and Stokoe II, K. H. (2000). “Liquefaction Resistance of Soils from Shear-Wave Velocity”, *J. Geotech. Geoenv. Eng.*, Vol. 126, No. 11, pp. 1015-1025.
2. Boulanger, R.W. and Idriss, I.M. (2014). “CPT and SPT Based Liquefaction Triggering Procedures”, *Rep. No. UCD/CGM.-14. Univ. of California, Davis, CA*.
3. Boulanger, R.W. and Idriss, I.M. (2015). “Magnitude Scaling Factors in Liquefaction Triggering Procedures”, *Soil Dyn. Earthq. Eng.*, Vol. 79, pp. 296-303.
4. Boulanger, R.W. and Idriss, I.M. (2016). “CPT-Based Liquefaction Triggering Procedure”, *J. Geotech. Geoenv. Eng.*, Vol. 142, No. 2, pp. 04015065.
5. Chang, W.J. (2011). “Evaluation of Undrained Shear Strains in Multi-Directional Horizontal Shaking” *Soil Dyn. Earthq. Eng.,* Vol. 31, No. 7, pp. 906-920.
6. Cetin, K.O. and Bilge, H.T. (2012). “Cyclic Large Strain and Induced Pore Pressure Models for Saturated Clean Sands”, *J. Geotech. Geoenv. Eng.*, Vol. 138, No. 3, pp. 309-323.
7. Cetin, K.O., Seed, R.B., Kayen, R.E., Moss, R.E.S., Bilge, H.T., Ilgac, M. and Chowdhury, K. (2018). “SPT-Based Probabilistic and Deterministic Assessment of Seismic Soil Liquefaction Triggering Hazard”, *Soil Dyn. Earthq. Eng.,* Vol. 115, pp. 698–709.
8. Cubrinovski, M., Rhodes, A., Ntritsos, N. and Ballegooy, S. Van. (2019). “System Response of Liquefiable Deposits”, *Soil Dyn. Earthq. Eng.,* Vol. 124, pp. 212–229.
9. Dadashiserej, A., Jana, A., Stuedlein, A.W. and Evans, T.M. (2022a). “Effect of Strain History on the Monotonic and Cyclic Response of Natural and Reconstituted Silts”, *Soil Dyn. Earthq. Eng.*, Vol. 160, pp. 107329.
10. Dadashiserej, A., Jana, A., Ortiz, S.C., Walters, J.J., Stuedlein, A.W. and Evans, T.M. (2022b). “Monotonic, Cyclic, and Post-Cyclic Response of Willamette River Silt at the Van Buren Bridge”, *In Geo-Congress 2022: Geophysical and Earthquake Engineering and Soil Dynamics, GSP No. 334, ASCE, Reston, VA,* pp. 431-443.
11. Dadashiserej, A., Jana, A., Xu, Z., Stuedlein, A.W., Evans, T.M., Stokoe II, K.H. and Cox, B.R. (2024a). “Dynamic Response of a Low Plasticity Silt Deposit: Comparison of *In-situ* and Laboratory Responses”, *Canadian Geotechnical J.*, Vol. 61, No. 7, pp. 1399-1417.
12. Dadashiserej, A., Jana, A., Stuedlein, A.W. and Evans, T.M. (2024b). “Cyclic Resistance Models for Transitional Silts with Application to Subduction Zone Earthquakes”, *J. Geotech. Geoenv. Eng.*, Vol. 150, No. 2, pp. 04023135.
13. Dobry, R., and Abdoun, T. (2015). “Cyclic Shear Strain Needed for Liquefaction Triggering and Assessment of Overburden Pressure Factor Kσ”, *J. Geotech. Geoenv. Eng.,* Vol. 141, No. 11, pp. 04015047.
14. Dobry, R., Ladd, R.S., Yokel, F.Y., Chung, R.M. and Powell, D. (1982). “Prediction of Pore Water Pressure Buildup and Liquefaction of Sands During Earthquakes by the Cyclic Strain Method”, *Gaithersburg, MD: National Bureau of Standards*, Vol. 138, pp. 150.
15. Esposito, M.P., Andrus, R.D. and Camp., W.M. 2014. “Ground Freezing and Sampling of Pleistocene Sand Near Charleston, South Carolina”, *J. Geotech. Geoenviron. Eng.,* Vol. 140, No. 1, pp. 185–193.

16. Idriss, I.M. and Boulanger, R.W. (2006). “Semi-Empirical Procedures for Evaluating Liquefaction Potential during Earthquakes”, *Soil Dyn. Earthq. Eng.,* Vol. 26, No. 2-4, pp. 115-130.
17. Idriss, I.M. and Boulanger, R.W. (2008). “Soil Liquefaction during Earthquakes”, *In: EERI Monograph No. 12, Earthquake Engineering Research Institute*, pp. 237.
18. Ishihara, K. (1968). “Propagation of Compressional Waves in a Saturated Soil”, *Proc., Int. Symp. Wave Prop. Dyn. Prop. Earth Matls.,* pp. 195-206.
19. Jana, A. (2021). “Use of Controlled Blasting to Quantify the Dynamic, *In-Situ*, Nonlinear Inelastic Response of Soils”, *Ph.D. Thesis, Oregon State University*.
20. Jana, A. and Stuedlein, A.W. (2021a). “Dynamic, *In-situ*, Nonlinear-Inelastic Response of a Deep, Medium Dense Sand Deposit”, *J. Geotech. Geoenv. Eng.,* Vol. 147, No. 6, pp. 04021039.
21. Jana, A. and Stuedlein, A.W. (2021b). “Monotonic, Cyclic and Post-Cyclic Response of an Alluvial Plastic Silt Deposit”, *J. Geotech. Geoenv. Eng.,* Vol. 147, No. 3, pp. 04020174.
22. Jana, A. and Stuedlein, A.W. (2022). “Dynamic, *In-situ*, Nonlinear-Inelastic Response and Post-Cyclic Strength of a Plastic Silt Deposit”, *Canadian Geotechnical J.,* Vol. 59, No. 1, pp. 111-128.
23. Jana, A., Dadashiserej, A., Stuedlein, A.W. and Evans, T.M. (2025). “Effect of Repeated Cyclic Straining on Dynamic Properties of Silts from Elemental and *In-situ* Tests”, *Proceedings, 8th Int. Conf. Recent Advances in Geot. Earthquake Eng. Soil Dynamics, 11-14 December 2024, IIT Guwahati, India*.
24. Jana, A., Dadashiserej, A., Zhang, B., Stuedlein, A.W., Evans, T.M., Stokoe II, K.H. and Cox, B. (2023). “Multi-directional VibroSeis Mobile Shaking and Controlled Blasting to Determine the *In-situ* Dynamic Response of a Low Plasticity Silt Deposit”, *J. Geotech. Geoenv. Eng.,* Vol. 149, No. 3, pp. 04023006.
25. Jana, A., Donaldson, A.M., Stuedlein, A.W. and Evans, T.M. (2021). “Deep, *In-situ* Nonlinear Dynamic Testing of Soil with Controlled Blasting: Instrumentation, Calibration, and Example Application to a Plastic Silt Deposit”, *Geotechnical Testing J.,* Vol. 44, No. 5, pp. GTJ20190426.
26. Kayen, R., Moss, R., Thompson, E., Seed, R., Cetin, K., Kiureghian A., Tanaka, Y. and Tokimatsu, K. (2013). “Shear-Wave Velocity–Based Probabilistic and Deterministic Assessment of Seismic Soil Liquefaction Potential”, *J. Geotech. Geoenviron. Eng.,* Vol. 139, No. 3, pp. 407–419.
27. KGW (2021). “Researchers Help Prepare Portland International Airport for when 'The Big One' Hits”, *National Broadcasting Company (NBC) affiliate station KGW8, Portland, OR. July 8 2021*.
28. Martin, G.R., Finn, W.D.L. and Seed, H.B. (1975). “Fundamentals of Liquefaction under Cyclic Loading”, *J. Geotech. Eng. Div.,* Vol. 101, No. 5, pp. 423–438.
29. Olaya, F.R. and Bray, J.D. (2022). “Strain Potential of Liquefied Soil”, *J. Geotech. Geoenv. Engrg.,* Vol. 148, No. 11, pp. 04022099.
30. Pyke, R., Seed, H.B. and Chan, C.K. (1975). “Settlement of Sands under Multi-Directional Shaking”, *J. Geotech. Eng.,* Vol. 101, No. 4, pp. 379-400.
31. Rathje, E.M., Phillips, R.D., Chang, W.J. and Stokoe II, K.H. (2001). “Evaluation Nonlinear Soil Response *In Situ*”, *Paper No. 1.61, 4th Int. Conf. Rec. Adv. Geotech. Earthq. Eng. Soil Dyn., University of Missouri—Rolla*, pp. 6.
32. Sanchez-Salinero, I., Roesset, J.M. and Stokoe, K.H. (1986). “Analytical Studies of Wave Propagation and Attenuation”, *Washington, DC: Air Force Office of Scientific Research*.
33. Seed, H.B., Idriss, I.M. and Arango, I. (1983). “Evaluation of Liquefaction Potential using Field Performance Data”, *J. Geotech. Eng.,* Vol. 109, No. 3, pp. 458-482.
34. Seed, H.B., Pyke, R. and Martin, G.R. (1978) “Effect of Multi Directional Shaking on Pore Pressure Development in Sands”, *J. Geotech. Eng.,* Vol. 104, No. 1, pp. 27-44.
35. Stuedlein, A.W., Jana, A., Dadashiserej and Yang, X. (2023). “On the *In-situ* Cyclic Resistance of Natural Sand and Silt Deposits”, *J. Geotech. Geoenv. Engrg.,* Vol. 149, No. 4, pp. 04023015.
36. Stokoe, K., Cox, B., Clayton, P. and Menq, F. (2017). “NHERI@ UTEXAS Experimental Facility: Large-Scale Mobile Shakers for Natural-Hazards Field Studies”, *16th World Conf. Earthq. Eng.,* pp. 9-13.

37. Verma, P., Seidalinova, A. and Wijewickreme, D. (2019). "Equivalent Number of Uniform Cycles Versus Earthquake Magnitude Relationships for Fine-Grained Soils", *Can. Geotech. J.*, Vol. 56, No. 11, pp. 1596–1608.
38. Zhang, B. (2020). "Improvements to Field Liquefaction Testing with Large Mobile Shakers", *Ph.D. thesis, Dept. of Civil, Architectural, and Environmental Engineering, Univ. of Texas*.